Spatiotemporal Evolution of Ground-Motion Intensity at the Irpinia Near-Fault Observatory, Southern Italy

Matteo Picozzi[*1], Fabrice Cotton[2,3], Dino Bindi[2], Antonio Emolo[1], Guido Maria Adinolfi[4], Daniele Spallarossa[5], and Aldo Zollo[1]

ABSTRACT

Fault zones are major sources of hazard for many populated regions around the world. Earthquakes still occur unanticipated, and research has started to observe fault properties with increasing spatial and temporal resolution, having the goal of detecting signs of stress accumulation and strength weakening that may anticipate the rupture. The common practice is monitoring source parameters retrieved from measurements; however, model dependence and strong uncertainty propagation hamper their usage for small and microearthquakes. Here, we decipher the ground motion (i.e., ground shaking) variability associated with microseismicity detected by dense seismic networks at a near-fault observatory in Irpinia, Southern Italy, and obtain an unprecedentedly sharp picture of the fault properties evolution both in time and space. We discuss the link between the ground-motion intensity and the source parameters of the considered microseismicity, showing a coherent spatial distribution of the ground-motion intensity with that of corner frequency, stress drop, and radiation efficiency. Our analysis reveals that the ground-motion intensity presents an annual cycle in agreement with independent geodetic displacement observations from two Global Navigation Satellite System stations in the area. The temporal and spatial analyses also reveal a heterogeneous behavior of adjacent fault segments in a high seismic risk Italian area. Concerning the temporal evolution of fault properties, we highlight that the fault segment where the 1980 M_S 6.9 Irpinia earthquake nucleated shows changes in the event-specific signature of ground-motion signals since 2013, suggesting changes in their frictional properties. This evidence, combined with complementary information on the earthquake frequency–magnitude distribution, reveals differences in fault segment response to tectonic loading, suggesting rupture scenarios of future moderate and large earthquakes for seismic hazard assessment.

KEY POINTS

- We decipher ground-motion intensity variability associated with microseismicity in south-central Italy.
- Ground-motion intensity shows an annual cycle in agreement with independent geodetic displacement observations.
- Our analyses reveal heterogeneous behavior of adjacent fault segments in an area with high seismic risk.

Supplemental Material

INTRODUCTION

Our understanding of physical processes occurring within seismogenic volumes is hampered by the impossibility of collecting measurements directly at the seismic source (*Ben-Zion*, 2019). Inferences about spatial and temporal dynamics of source processes can be obtained by either analyzing their effects on mechanical properties of rock, such as seismic velocity, or by retrieving source parameters through the inversion of seismic data. Tectonic stress accumulation and progressive weakening of active faults are accompanied by seismic velocity changes and micro cracking (*Nielsen*, 2017). Therefore, velocity changes from seismic noise (*Brenguier et al.*, 2008), repeated seismic sources measurements (*Uchida and Bürgmann*, 2019), and estimates of source parameters of microearthquakes (*Allmann and Shearer*, 2007) are routinely performed and retrospectively analyzed to capture any preparatory process anticipating large earthquakes. Existing approaches, however, suffer from the lack of long-duration near-fault observations, the limited spatial resolution of tomographic images, and the fact that important source parameters such as energy and stress drop (Scholz, 2019) are difficult to estimate and are affected by large uncertainties (*Cotton et al.*, 2013).

In recent years, the decomposition of the ground-motion residuals into source, path, and site-specific

1 Department of Physics, University of Naples Federico II, Naples, Italy

2 German Research Centre for Geosciences, Potsdam, Germany

3 Institute for Earth and Environmental Sciences, University of Potsdam, Potsdam, Germany

4 Department of Science and Technology, University of Sannio, Benevento, Italy

5 Dipartimento di Scienza della Terra, dell'Ambiente e della Vita, University of Genova—DISTAV, Genoa, Italy

*Corresponding author: matteo.picozzi@unina.it

terms became of interest for a wide spectrum of applications (*Al Atik et al.*, 2010; *Baltay et al.*, 2017). A common application of such an approach is for the development of ground-motion prediction equations (GMPEs), which are typically used to compute both the median predictions and the aleatory variability for any seismic scenario of interest (e.g., *Douglas and Edwards*, 2016; *Kotha et al.*, 2020). Furthermore, the ground-motion model residuals decomposition analysis also has been used for investigating the fault healing (*Bindi et al.*, 2018), the preparation phase of earthquake nucleation (*Piña-Valdés, Socquet, and Cotton*, 2018; *Picozzi, Bindi, Zollo, et al.*, 2019) and even onsite early warning applications (*Spallarossa et al.*, 2019; *Iaccarino et al.*, 2020).

In the decomposition of ground-motion residuals, the observed ground motion is corrected for the earthquake size, as measured by the moment magnitude (M_w), and for the scaling with distance using a reference GMPE median model. Then, the remaining variability, typically still more than one order of magnitude variable, is decomposed to isolate the earthquake-specific contribution (*Bindi et al.*, 2004; *Al Atik et al.*, 2010; *Piña-Valdés, Socquet, and Cotton*, 2018; *Piña-Valdés, Socquet, Cotton, and Specht*, 2018). The source term, referred to as "delta between-event term" δBe (*Al Atik et al.*, 2010), allows for tracking ground-shaking anomalies generated by changes in the source characteristics that impact on the ground shaking but are not captured by the magnitude and distance scaling (calibrated locally) that define the reference model. Thus, δBes incorporate the effects of multiple physical processes, such as stress drop, source-near frictional properties, and source volume rheology (*Causse and Song*, 2015; *Bindi et al.*, 2017). Importantly, δBe s are independent of the theoretical rupture models assumed to compute source parameters such as stress drop. Therefore, δBes are free from the epistemic uncertainties typical of parameters such as stress drop derived by rupture model-based approaches (*Piña-Valdés, Socquet, and Cotton*, 2018; *Piña-Valdés, Socquet, Cotton, and Specht*, 2018). We will continue discussing this aspect later. In this work, we show that by analyzing near-fault ground-motion recordings of micro and small earthquakes, it is possible to resolve source heterogeneities within the source volume and to follow their evolution over time.

The main characteristic of our approach is therefore to isolate earthquake-specific contributions (i.e., the δBes) to the distribution of ground-motion residuals computed with respect to a reference model. We

follow a common practice in the context of seismic hazard assessment (*Bindi et al.*, 2017), we use a standard nomenclature (*Al Atik et al.*, 2010) to define our reference model in terms of magnitude and distance scaling, and we apply a mixed effect regression (*Bates et al.*, 2015; *Kotha et al.*, 2016; *Bindi et al.*, 2018) considering both the earthquake population and the set of recording stations as grouping levels.

In this study, we consider δBe to be an observable parameter of an intraplate crustal fault system, and we show that δBe allows changes in the dynamic characteristics of rupture processes to be mapped in space and followed in time.

We prove the enlightening power of the δBes by analyzing micro and small earthquakes generated by an active and densely monitored fault in southern Italy, where strong historical earthquakes (i.e., 1561 M_w 6.4, 1694 M_w 6.9, 1826 M_w 5.7, 1853 M_w 5.9, and 1857 M_w 7.0) and the most recent 1980 M_S 6.9 Irpinia earthquake (*Bernard and Zollo*, 1989) occurred.

The tectonic complexity of the Irpinia region is well known (e.g., *Bernard and Zollo*, 1989; *Ascione et al.*, 2013; *Adinolfi et al.*, 2019), it is characterized by active, extensional faults arranged in subparallel structures, mainly disseminated over the Apennines axial sector, with trends mainly ranging from west-northwest–east-southeast to northwest–southeast. In Irpinia, the seismic active rock volume consists of the Apulian Platform carbonates and its basement. The background microseismicity here is partially controlled by fluids of different origin (e.g., *Chiodini et al.*, 2004; *Amoroso et al.*, 2014; *Improta et al.*, 2014; *D'Agostino et al.*, 2018).

We measure δBe for ~3000 earthquakes with local magnitudes (M_L) between M_L 0 and 4.2 (i.e., moment magnitude M_w, between 0.3 and 3.8) that have occurred between 2008 and 2020 within a buffer of ±30 km along the Irpinia fault system (*Picozzi, Bindi, Zollo, et al.*, 2019; *Picozzi et al.*, 2021). In the first part of this work, we analyze the spatial distribution δBe. Our images of the δBe spatial distribution allow for illuminating fault segments characterized by different dynamics. These images complement well those of the cumulative frequency–magnitude (CFM) distribution computed for same dataset, those of the spatial distribution of $V_P = V_S$ observations (*Amoroso et al.*, 2014; *Improta et al.*, 2014, 2019) and those derived using source parameter estimates from the companion work to this study (e.g., stress drop, corner frequency, fracture energy, and radiation efficiency from *Picozzi et al.*, 2021).

D'Agostino et al. (2018) analyzed the temporal evolution of geodetic displacement measurements and showed that the karst aquifers in the Irpinia area, the largest in the Apennines (*Fiorillo et al.*, 2015), play a crucial role in modulating the crustal deformation and the associated microseismicity. *Picozzi et al.* (2021) found that the poro-elastic deformation perturbation generated by the karst aquifer recharge is modulating not only the occurrence rate of microseismicity but also can lead to rupture asperities with different sizes and characteristics. It is worth mentioning that, for the Apennine chain, the relevance of pore pressure variations within fluid-filled cracks in driving background seismicity and promoting the nucleation of large earthquakes is well documented (e.g., *Lucente et al.*, 2010; *Improta et al.*, 2014; *Sugan et al.*, 2014; *Chiarabba et al.*, 2020).

In the second part of this work, we investigate the temporal evolution of δBe for both peak ground acceleration (PGA) and Fourier amplitude spectrum (FAS) at different frequencies, in comparison with measurements of geodetic displacement (from *D'Agostino et al.*, 2018), stress drop ($\Delta\sigma$, from *Picozzi et al.*, 2021), and the number of earthquakes, looking for possible changes in ground-motion intensity, which could hint at changes in the behavior of the Irpinia faults system.

DATASET

We take advantage of an existing natural laboratory for studying fault evolution and rupture processes, the Irpinia near-fault observatory (INFO; *Zollo et al.*, 2014), in southern Italy. INFO consists of the Irpinia seismic network (ISNet, see Data and Resources), a dense network of 32 seismic stations distributed over an area of about 100 km × 70 km (Fig. 1a) and operational since 2008.

We analyze about 36,200 acceleration and velocity waveforms from 3016 earthquakes with local magnitudes (M_L) between M_L 0 and 4.2 and recorded by at least three stations in the range of 2–100 km. Figure 1b shows the comparison between the Caposele spring discharge and the number of earthquakes with magnitude above the completeness magnitude M_c per year recorded in the Irpinia area. As discussed by *D'Agostino et al.* (2018), the Caposele spring provides important information concerning the underlying aquifer in fractured Mesozoic limestones because it is not affected by anthropogenic modifications in its catchment. These authors also showed that the Global

Navigation Satellite System (GNSS) stations provide a clear overview of the karst aquifers deformation. Therefore, in this study, we compare ground-motion intensity with the geodetic displacement time series from the GNSS stations MCVR and MRLC (*Avallone et al.*, 2010), which data have been preprocessed by *D'Agostino et al.* (2018).

Uncertainties in event locations (*De Landro et al.*, 2015) are mostly within 1 km both horizontally and vertically (i.e., the median error in location is ~0.5 km). The magnitude versus hypocentral distance scatter plot of the dataset analyzed in this study (Fig. 1c) shows that the dataset is dominated by microearthquakes with M_L between 0.5 and 2. The completeness magnitude M_c over the years has been quite stable around M_L 1 (Fig. 1d; defined by the software package ZMAP, *Wiemer*, 2001), in agreement with the M_L 1.1 estimate proposed by *Vassallo et al.* (2012).

METHODS

Seismogram processing

Processing is carried out on velocimetric records sampled at 125 Hz after their deconvolution for the instrumental response and filtering on the 0.5–40 Hz band. Then, the PGA is estimated for each component after recordings differentiation.

For the FAS computation, which are used to estimate the seismic source parameters, we follow *Picozzi, Bindi, Zollo, et al.* (2019) and *Picozzi et al.* (2021). The selection of the S-wave time window for FAS computation is done following a procedure proposed by *Pacor et al.* (2016) that allows for automatically selecting a portion of signals dominated by S waves and has become standard for analyses at the local scale. In particular, we consider time windows starting 0.1 s before the S-wave onset and for each record ending at a different percentile of the cumulative distribution of the squared velocity integrals as a function of the source to site distance R: (1) 90th percentile when $R < 25$ km, (2) 80th percentile when 25 km $< R < 50$ km, and (3) 70th percentile when $R > 50$ km. For FAS calculation, we impose a minimum duration of 5 s and a maximum duration of 20 s. For each recording, a signal-to-noise ratio (SNR) is evaluated by considering a pre-event noise window of the same length as the signal window. FAS are smoothed by a filter with variable frequency band equal to 25% of the central frequency. Finally, data are extracted with the following criteria: hypocentral distance between 5
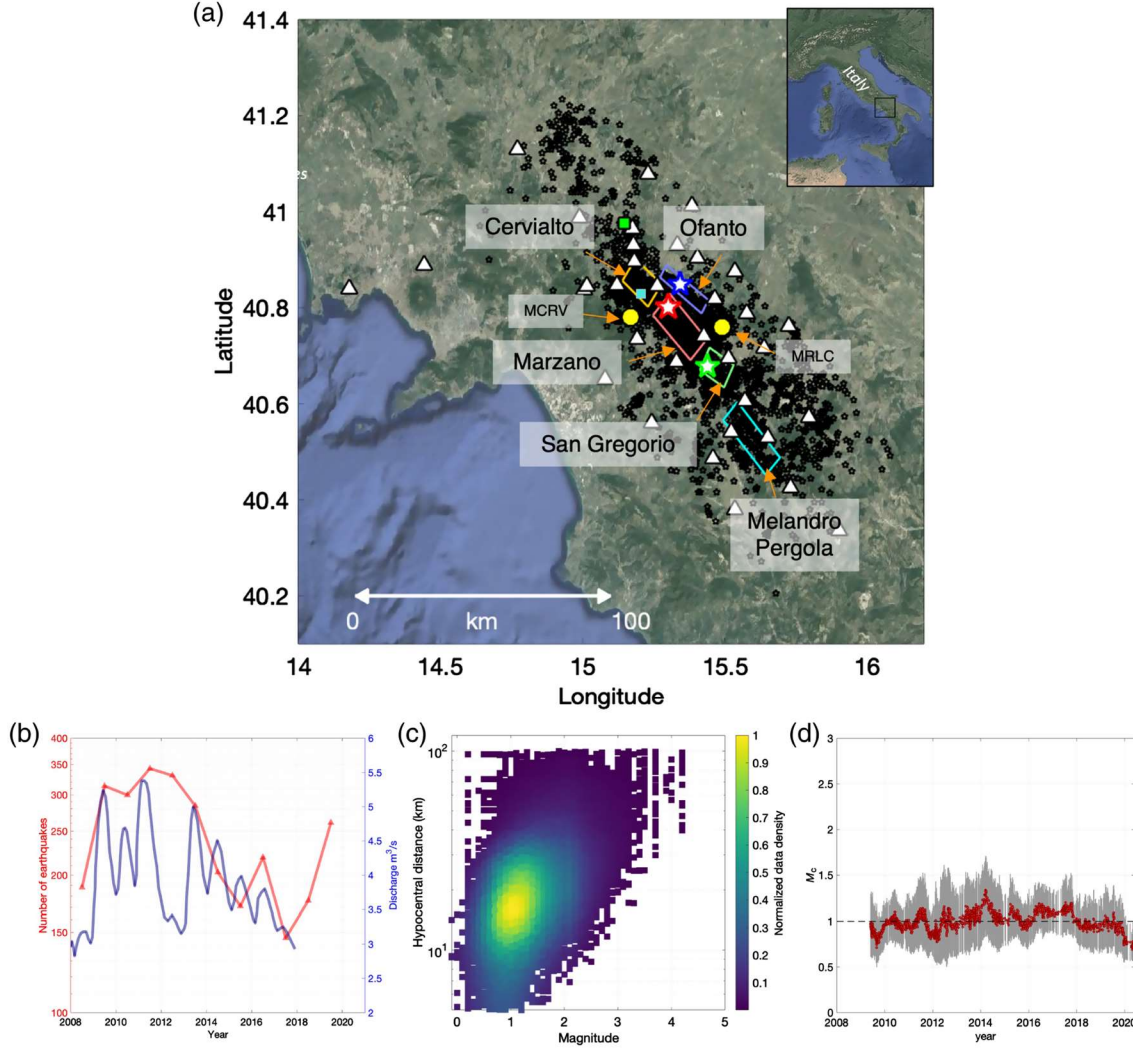
Figure 1 *(a) Locations of the earthquakes considered in this study (black stars), Irpinia Seismic Network (ISNet) seismic stations (white triangles), Global Navigation Satellite System (GNSS) stations (yellow dots), CO2 degassing site Mefite d'Ansanto (green square), and Caposele spring (cyan square). Projection of seismogenic sources: Cervialto fault (C-fault, yellow line), Marzano fault (M-fault, red line), San Gregorio fault (SG-fault, green line), Ofanto fault (O-fault, blue line), and Melandro-Pergola fault (MP-fault, cyan line). The 1980 M_w 6.9 Irpinia earthquake was characterized by three main rupture segments, nucleating at 0 s (red star), 20 s (green star), and 40 s (blue star). The map was made using MATLAB (R2019b; see Data and Resources). (b) Number of events per year above the magnitude of completeness (red line) and spring discharge of the Caposele spring (blue line; digitized by D'Agostino et al., 2018). (c) Density plot normalized between 0 and 1 of the moment magnitude versus hypocentral distance for the recordings analyzed in this study. (d) Temporal distribution of completeness magnitude ±1 standard deviation. The color version of this figure is available only in the electronic edition.*

and 100 km, events recorded by a minimum of three stations, and SNR for the two horizontal components ≥ 10.

GMPE and between event residuals δBe estimation

We develop a GMPE for the Irpinia area following a well-established approach (*Bindi et al.*, 2017), applying a random effect strategy (*Bates et al.*, 2015; *Kotha et al.*, 2016; *Bindi et al.*, 2018).

$$\log(Y) = e1 + e2\left(M - M_{ref}\right) + e3\left(M - M_{ref}\right)^2 + e3\log R_{hypo} + e4 R_{hypo} + \delta Be + \delta S2S + \varepsilon \quad (1)$$

in which Y is either the geometrical mean of the two horizontal PGA ($m = s^2$) or of the amplitude FAS at frequency f and M_{ref} is the reference magnitude set equal to 1.5.

The GMPE is calibrated for moment magnitude (M_w), provided by *Picozzi et al.* (2021), and using the

hypocentral distance R_{hyp} (in kilometers) up to 100 km. Besides the model coefficients (i.e., e1, e2, and e3), the model in equation (1) contains three random effects: (1) δBe is the between-event distribution that measures the systematic deviation from the median of each group of recordings for the same event; (2) $\delta S2S$ is the between-station residual distribution measuring the systematic deviation from the median of the recordings relevant to the same station; and (3) finally, ε is the single-station within-event residual.

In practice, the $\delta S2S$ term (shown in Fig. S1, available in the supplemental material to this article) describes the site amplification effects, whereas ε is the left-over variability (see *Al Atik et al.*, 2010 for a comprehensive glossary of terms describing the components of the ground-motion variability in the context of probabilistic seismic hazard assessment).

In this study, we focus on δBe residuals and their connection with the seismological parameters derived following *Picozzi et al.* (2021). As previously discussed, to estimate source parameters such as the stress drop $\Delta\sigma$, we need to assume a theoretical source model (e.g., *Brune*, 1970; *Madariaga*, 1976). By assuming a rupture model, we introduce into our results an epistemic uncertainty because we can never be sure that the selected model is compliant with the real rupture (the model is inevitably our simplified view of a rather complex natural phenomena). Contrariwise, when we estimate δBe, we do not need to introduce any theoretical rupture model; we only correct the observation (e.g., PGA or FAS amplitude) for the magnitude and distance scaling relevant to a ground-motion model calibrated for the area of interest. The δBe distribution is describing event-specific characteristics of the observation minus prediction residuals, that is, they provide information about the importance of event-specific deviations from the median prediction as determined by the assumed magnitude and distance scaling. In other words, variability of source parameters not accounted for by the median model is mapped into the between events, whereas station-specific or path-specific contributions are accounted for by other residual components. Examples are errors in the source-related explanatory variables, or the variability of source parameters that have an impact on the considered ground-motion parameter, but they are not included in the ground-motion model defining the median prediction. For example, if a wrong magnitude value has been assigned to one specific earthquake, then all recordings of that specific event will show biased predictions (e.g., PGA larger or lower than the median). Another example is the case of a source parameter (e.g., $\Delta\sigma$) that has an impact on the considered intensity measure (e.g., PGA or FAS), but it is not included as independent variable for the median model (because of the difficulty of predicting $\Delta\sigma$ of future earthquakes and its strong model dependence). We are interested in the latter case: we use the δBe residuals to isolate in the residual distributions' repeated source effects, and we look for correlations with source parameters (computed for the assumed rupture model) to prove that we can image the spatial and temporal variability of source processes occurring in the region of interest by monitoring the between-event behavior.

The results of the regression analysis for equation (1) are provided in the supplemental material. Furthermore, the supplemental material also includes the temporal evolution of the δS2S term for each station.

Nested random effects

We also develop an additional GMPE by nesting δBe into the between-cluster random effects (*Rabe-Hesketh et al.*, 2005) to assess the systematic deviation from the overall median prediction of different sets of recordings grouped by clusters of earthquakes.

The nested GMPE model takes the form

$$
\begin{aligned}
\log(Y) = e1 &+ e2\big(M - M_{ref}\big) + e3\big(M - M_{ref}\big)^2 \\
&+ e3 \log R_{hypo} + e4 R_{hypo} \\
&+ (1|\delta B_{CL}/\delta B_e) + \delta S2S + \varepsilon
\end{aligned}
\tag{2}
$$

Thus, equation (2) differs from equation (1) by introducing an additional grouping level (i.e., $1|\delta B_{CL}/\delta B_e$, in which δB_{CL} indicates the between-cluster distribution and the symbol "/" means that the δBe are nested within the between clusters δB_{CL}). In simple terms, the events are divided into 100 spatial clusters by a K-means clustering approach (*Pedregosa et al.*, 2011) after having normalized the hypocentral coordinates between 0 and 1. Therefore, because in equation (2) the δBe for events associated with a cluster are nested within the δB_{CL}, these latter parameters allow us to highlight if a group of events occurring in a specific crustal volume has, on average, radiative properties different from those occurring in other areas. The result of the regression analysis for equation (2) is provided in the supplemental material.

A detailed review of the adopted symbols used in equations (1) and (2) can be found in *Bates et al.* (2015).
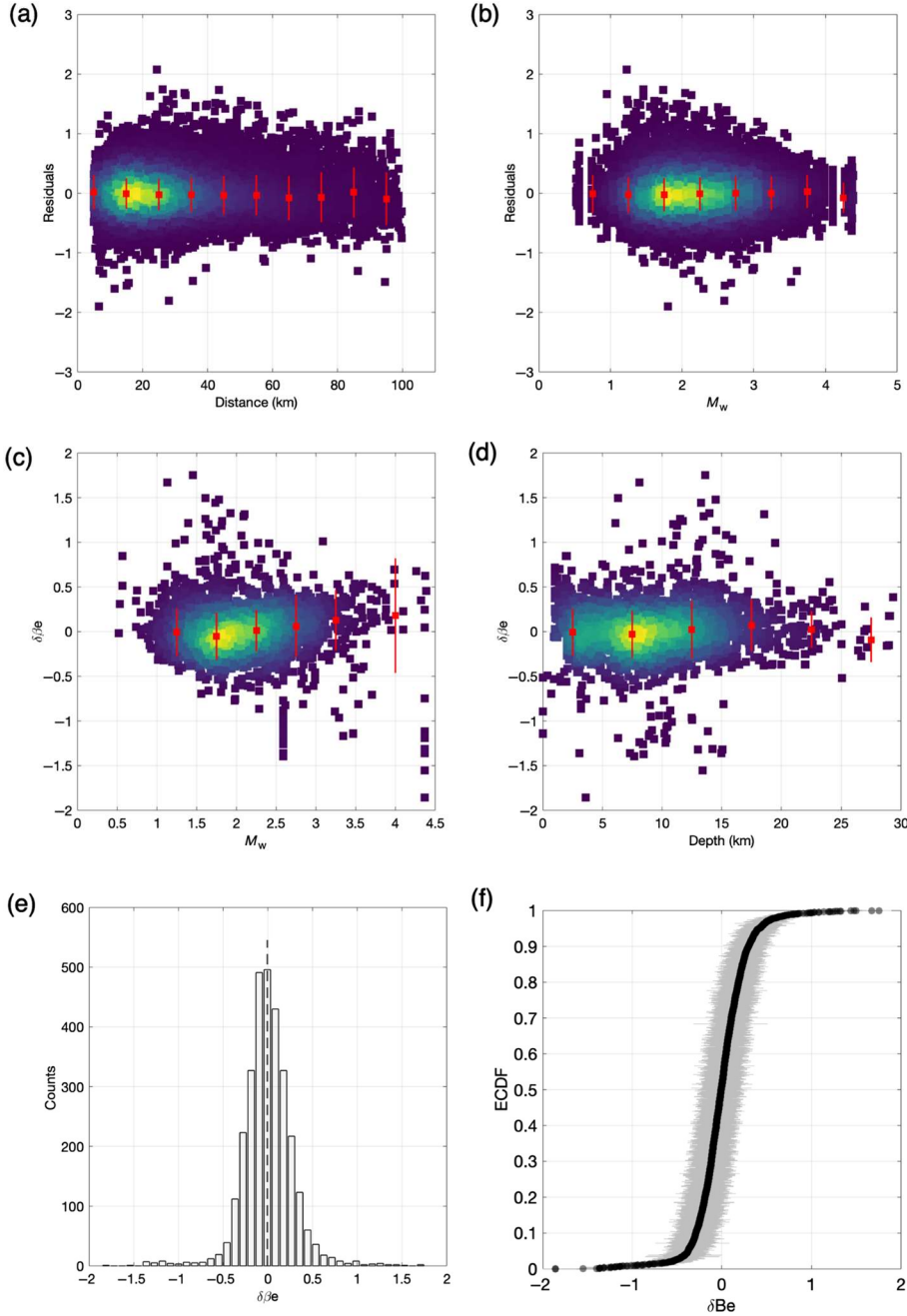
Figure 2 *(a) Density plot normalized between 0 and 1 for the within event residuals (ε) versus hypocentral distance, median (red squares), and standard deviation (red lines) of ε computed for bins of residuals in hypocentral distance (viridis color scale with yellow for higher density of data as in Fig. 1). (b) Same as (a) but for moment magnitude M_w. (c) Between event residuals (δBe) computed for peak ground acceleration (PGA) versus M_w, median (red squares) and standard deviation (red lines) of (δBe) computed for bins of values in hypocentral distance. (d) Same as (c) but for hypocentral depth. (e) δBe distribution. (f) ECDF for δBe. The color version of this figure is available only in the electronic edition.*

b-value

The analysis of the CFM distributions to estimate the b-value of the Gutenberg–Richter law (*Gutenberg and Richter*, 1942):

$$\log(N) = a - bM_w \qquad (3)$$

in which N is the cumulative number of earthquakes and a and b are parameters describing the productivity and relative event size distribution, respectively, is carried out using the whole magnitude-range method implemented in the software package ZMAP (*Wiemer*, 2001) and allows for the simultaneous estimation of the completeness magnitude M_c and of the parameters a and b (i.e., the latter is obtained by the maximum-likelihood approach; *Aki*, 1965). The uncertainty of the obtained parameters is computed by means of a bootstrap approach (*Efron*, 1979). For each dataset, 10,000 realizations of random sampling with replacement are performed.

To map the *b*-value spatial distribution, we follow *Wiemer and Wyss* (2002) and apply a 3D gridding with

a 2 km step, having size 170 km × 120 km, with the major axis coinciding with the Irpinia fault strike, and considering depths between 1 and 29 km. For each node, we select events with distances within 15 km, and we parameterize equation (3). Nodes that have less than 200 events within 15 km are discarded.

Source parameters

The source parameters are derived by applying a generalized inversion technique (*Castro et al.*, 1990). Here, in terms of both data and analysis strategy, we follow *Picozzi et al.* (2021), with the only exceptions being that we consider a ω^γ source model and we invert the source spectra also for the parameter γ controlling the high-frequency spectral falloff. For the sake of readability, here we refer mainly to *Picozzi et al.* (2017, 2021) for the description of both the waveform analysis procedure and the details on the source spectra inversion for the estimation of corner frequency f_c, seismic moment M_0, stress drop $\Delta\sigma$, γ parameter, and radiation efficiency η_R, whereas a few details on the procedure are presented in the supplemental material. The comparison of the f_c and M_0 presented by *Picozzi et al.* (2021) and those derived in this study is shown in Figure S2.

RESULTS

Our analysis starts by considering the general characteristics of the δBes in terms of their spatial distribution and comparing them with those of the source parameters. Then, we analyze the δBes temporal evolution and compare them with the geodetic displacement of two GNSS stations (MRCV and MRLC) from *D'Agostino et al.* (2018).

Figure 2 shows the residual ε for recordings and the δBes for events obtained by parametrizing the ground-motion model in equation (1) using R_{hypo} and M as predictor variables. To highlight the eventual existence of trends in the distribution of residuals ε, we divide the range of hypocentral distances and magnitude in bins of 10 km and 0.5 magnitude units, respectively. Then, for each bin we assess the median and standard deviation of residuals. We repeat the analysis for δBes, but in this case, we include all events with magnitudes larger than M_w 3.5 into a unique bin given the scarcity of large magnitude events in our dataset.

Looking at the trend of ε, δBes, and their median values and considering the size of the standard deviation associated with values in each bin, we can conclude that there is no significant trend in the considered parameters with R_{hypo}, M, and hypocentral depth (Fig. 2a–d). Even considering the ε residuals for selected FAS frequencies (i.e., 1, 7.5, 12.5, and 25 Hz) as a function of the hypocentral distance, epicentral distance, and depth (Fig. S3), we do not observe significant trends, confirming the absence of a trade-off between event depths and epicentral distances.

As expected by construction, δBes approximate a zeromean normal distribution (Fig. 2e), with standard deviation indicated in the following as τ. Figure 2f shows the empirical cumulative probability distribution (ECDF) of δBe.
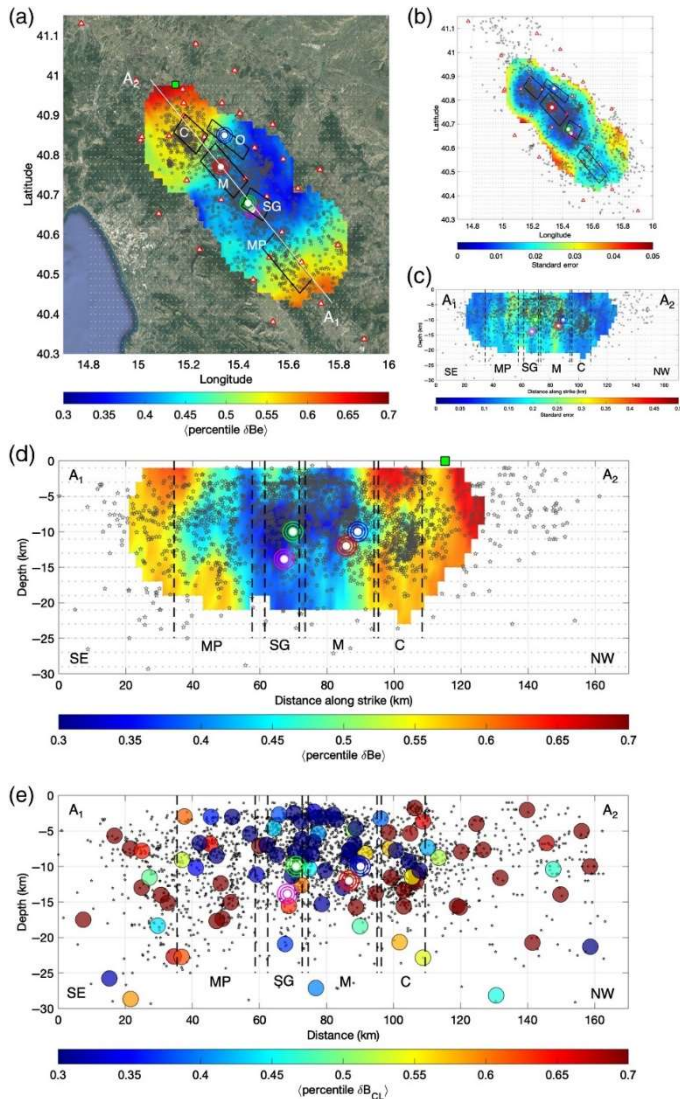
δBe spatial distribution

Similar to *Picozzi, Bindi, Zollo, et al.* (2019) and *Picozzi et al.* (2021), who investigated the spatial variability of source parameters in the Irpinia area, we map the spatial variability of δBe for events with magnitudes between M_w 1 and 2.5. This magnitude range is selected, according to *Picozzi et al.* (2021), to consider in our analyses the bulk of the datasets but discarding smaller and larger magnitude events that might have not been properly recorded in their source properties due to a limited frequency band (the former) or anomalous radiative properties due to runaway ruptures (the latter; as discussed by Kanamori and Heaton, 2000: with the increase in their size, earthquakes can progressively be influenced by melting and pressurization, which leads to a reduction of the frictional level and increase of the slip).

To map in space δBe, we follow an approach similar to that adopted for the b-value, in which we exploit the ECDF computed for the whole population of δBe. We consider a regular 3D grid with size 2 km. For each grid node, we select events within a maximum distance of 10 km. Then, we associate with each selected event the percentile of the global ECDF corresponding to its δBe. Finally, we assign the average of associated percentiles (divided by 100) to the considered node and indicate it as <percentile δBe>. Therefore, <percentile δBe> provides a first-order information about which part of the whole population ECDF is sampled by events occurring in the proximity of each node.

Clearly, in case of a uniform spatial distribution of δBes, the resulting <percentile δBe> maps would appear homogenous (with values around 0.5), whereas an inhomogeneous spatial distribution of δBe will result in <percentile δBe> maps with areas characterized by values smaller or larger than 0.5.

Figure 3 (a) Map showing the spatial distribution for the average of percentiles (divided by 100) of δBe associated with each grid node (gray dots) of the mesh considered in the investigated area. ISNet stations (white triangles with red edge). Earthquake epicenters (gray stars) and faults projection (black lines). Epicenters of the nucleation point for the 1980 M_w 6.9 Irpinia earthquake (dots with circles colored as in Fig. 1a) and epicenter of the 1996 M_w 5.1 Irpinia earthquake (fuchsia dots with circles). (b) Same as (a) but for the standard error of δBe. (d) Same as (a) but for a cross section along the strike direction (section A–A′ in a), fault sectors (dashed line). (c) Same as (d) but showing the standard error from bootstrap analysis for the cross section along strike direction. (e) Same as (b) but for the nested between-cluster residuals (δB_{CL}). The color version of this figure is available only in the electronic edition.

As for the b-value maps, to favor the δBe spatial map robustness, we set the requirement of a rather high number of events associated with each node. Hence, nodes having less than 50 earthquakes within 10 km are discarded. Furthermore, all δBe maps are

generated using as the interpolating function the default shading mode in MATLAB, which does a linear interpolation of colors in each line segment and face by interpolating the color map index or true color value across the line or face.

We assess the robustness of results using a bootstrap approach (*Efron*, 1979). Compared with tomographic images of seismic wave velocity, the spatial distribution of δBe provides insights into the existence of event-specific anomalies for the Irpinia area that are fully data driven.

Figure 3 shows a plain view of the area and a cross section along the fault system strike, in which we observe significant lateral δBe variations. In this figure, we highlight the most significant fault segments in the area (Fig. 3a). Four out of five fault segments contributed to the 1980 M_w 6.9 Irpinia earthquake, a complex rupture episode characterized by three main ruptures that occurred within approximately one minute. During this strong earthquake, the rupture nucleated in the Marzano segment (M), propagated northern through the Cervialto segment (C), after 20 s caused the rupture of the southern San Gregorio segment (SG), and after 40 s caused the rupture of the eastern Ofanto segment (O) (*Pantosti and Valensise*, 1990). The fifth segment, the Melandro–Pergola segment (MP), is located south of SG, and it may have been the first rupture episode of the complex 1857 M_w 7.0 Val d'Agri earthquake and probably the epicentral area of the 1561 M_w 6.4 Vallo di Diano earthquake (*Burrato and Valensise*, 2008).

As shown in Figure 3a, d, the M and O segments in the central part of the investigated area are characterized by minima of the δBe distribution, whereas the C segment presents the highest values. Another striking aspect is the high δBe at the southern margin of MP.

We perform several analyses to assess the robustness of obtained images. First, we evaluate the uncertainties of δBe values aggregated to each grid node following a bootstrap approach (*Efron*, 1979). Figure 3b, c shows that, in correspondence of the considered fault segments, the standard error is generally lower than 0.1 and significantly smaller than the δBe anomalies. Next, we check whether the anomalies imaged by contouring δBe values persist even when the events are spatially grouped before the analysis. The δBe analysis is repeated considering clusters of events identified with a K-means clustering (*Pedregosa et al.*, 2011), and we study the between-cluster δB_{CL} random effects (*Rabe-Hesketh et al.*, 2005).
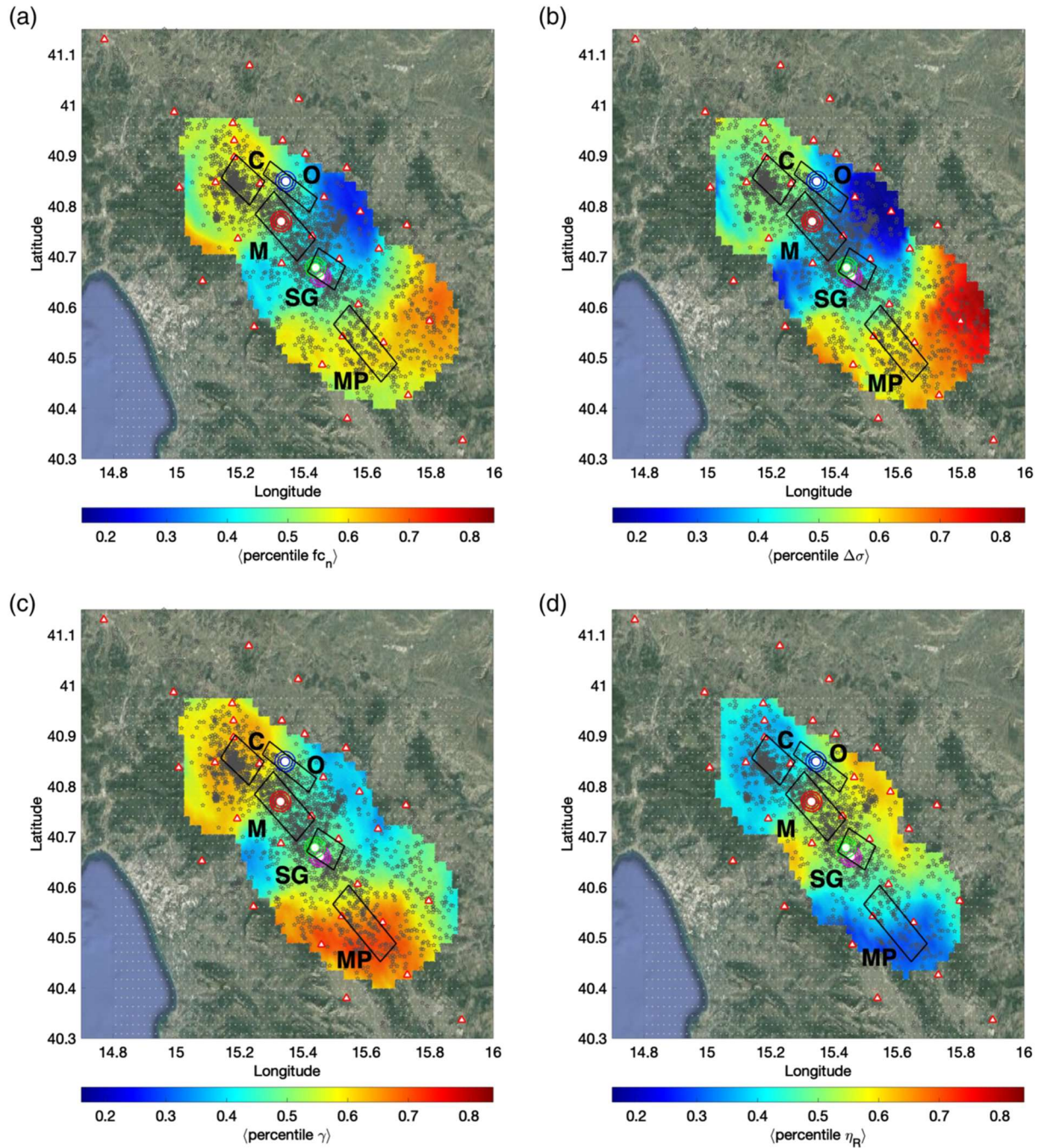
Figure 4 *(a) Map showing the spatial distribution for the average of percentiles associated with grid nodes for the normalized corner frequency f_{cn}. (b) Same as (a) but for stress drop $\Delta\sigma$. (c) Same as (a) but for the parameter γ controlling the high-frequency spectral falloff. (d) Same as (a) but for radiation efficiency η_R. The color version of this figure is available only in the electronic edition.*

Considering 100 clusters of earthquakes (Fig. S4), Figure 3e shows the ECDF values for the delta between cluster (δB_{CL}), and it confirms the heterogeneous structure of the fault system. Indeed, we observe in Figure 3e the same main features of the δBe spatial distribution (Fig. 3d), corresponding to high δB_{CL} values occurring in correspondence of the Cervialto (C)

and Melandro–Pergola (MP) fault segments, whereas the central Marzano (M) and San Gregorio (SG) segments show smaller ones.

The main features of the δBe spatial distribution persist even when we consider different magnitude thresholds (i.e., considering only events with magni-

tudes larger than M_w 1, 1.6, and 2, Fig. S5a–c, respectively). Finally, we also check whether δBe values are in trade-off with attenuation effects. For this purpose, we take fault C as an example, and we inspect ε for events that occurred in this segment (colored rays connecting earthquakes and stations in Fig. S6). The ε distribution shows no spatial trend, and considering that a large number of stations recorded these events at different distances, we have no evidence to support the presence of a trade-off between source and propagation effects. In conclusion, we consider the δBe anomalies shown in Figure 3 as robust features.

δBe spatial distribution versus other macroscopic source properties

As discussed by previous authors (e.g., *Bindi et al.*, 2007, 2017; *Cotton et al.*, 2013; *Causse and Song*, 2015; *Courboulex et al.*, 2016; *Oth et al.*, 2017), the ground-motion intensity is related to stress drop $\Delta\sigma$ and rupture velocity V_R variability.

Following *Kanamori and Rivera* (2004), we express this kind of connection between parameters through the expression:

$$\text{PGA} \propto f_c^n \propto \left(V_R \Delta\sigma^{\frac{1}{3}} M_0^{-3}\right)^n, \tag{4}$$

in which M_0 indicates the seismic moment and f_c means the corner frequency.

A connection between PGA and f_c is given using the random vibration theory (*Hanks and McGuire*, 1981) through the root mean square (rms) of the ground acceleration a_{rms} as follows:

$$\text{PGA} \propto f_c^{5/2} \sqrt{2 \ln(2 f_{max}/f_c)} \tag{5}$$

As shown in Figure S7, the exponent n of equation (4) approximating PGA values derived from equation (5) can be assumed to be close to 2, but a value of n equal to 2.4 as proposed by *Causse and Song* (2015) also allows for satisfactorily fitting the data. For our purpose, the exact value of coefficient n is not important; equation (4) provides a theoretical framework to interpret the variability of ground-motion intensity not only in terms of $\Delta\sigma$, as generally done, but in terms of f_c.

The spatial variability of $\Delta\sigma$, f_c, γ (i.e., the parameter controlling the high-frequency spectral falloff), and η_R (i.e., the radiation efficiency, *Kanamori and Heaton*, 2000) is computed following the same scheme adopted for δBe (Fig. 4). Because f_c scales with M_0, to represent its spatial distribution, we remove this dependence as follows: (1) we divide the M_0 range into 10 bins; (2) for each bin, we compute the average of f_c, $\langle f_c \rangle$; and (3) we compute the residuals between f_c and $\langle f_c \rangle$ relative to the M_0 bin in which it belongs. In this way, Figure 4a shows the spatial distribution in excess or deficient of the normalized corner frequency f_{cn}, with respect to the mean of its ECDF.

We observe that the main features of the δBe spatial distribution (i.e., the high anomaly in the northern and southern sectors and the low anomaly in the center of the Irpinia area) are present in both f_{cn} and $\Delta\sigma$ images (Fig. 4a, b). In addition to these observations, it is also worth noting the consistent spatial distributions for γ and η_R. These results suggest that the energy dissipation during rupture processes in the northern and southern areas is greater than in the central one. They also suggest that such dynamic variations leave an imprint in the ground-motion intensity that can be mapped by δBe.

The relation among the source parameters with δBe can also be perceived from Figure S8, in which we plot the parameter values associated with each node of the grid. In this way, we consider values resulting from the average of events spatially distributed close to a given node, but we avoid being influenced by the smoothing of the spatial images shown in Figure 4. Figure S8 shows the positive correlation of $\Delta\sigma$, f_{cn}, and γ with δBe and the negative correlation between δBe and η_R.

Equation (4) provides a general model to understand the connection between δBe and the considered source parameters, but deriving a formal link among them is not straightforward. We can consider the link between the critical slip weakening distance D_c with η_R through the coseismic slip D_S which is expressed as

$$\eta_R = 1 - \frac{D_c}{D_S}, \tag{6}$$

which derives from *Kanamori and Heaton* (2000) and the relation

$$f_c \propto -\frac{\Delta\sigma V_R}{\mu(D_S - D_c)}, \tag{7}$$

(i.e., equation S4 in the supplemental material).

Combining equations (6) and (7) with equation (4), we obtain

$$\delta Be_{\mathrm{PGA}} \propto -\left(\frac{\Delta\sigma V_R}{\mu D_S \eta_R}\right)^n, \qquad (8)$$

in which we associate the subscript PGA to δBe to highlight that equation (8) is derived for the PGA. It is worth noting that equation (8) highlights a clear trade-off between δBe and the source parameters, but at the same time, it shows the relationship between η_R and δBe as seen on the data (Figs. 3a and 4d). Future studies will be devoted to investigating the sensitivity of δBe to the different source parameters in equation (8). Here, we exploit equation (8), and in particular the relationship between η_R and δBe, to interpret the systematic spatial and temporal deviation of PGA values captured by δBe for the small earthquakes in Irpinia.

δBe temporal evolution

Previous studies have found that the temporal variability of ground shaking resembles temporal changes in stress drop (*Bindi et al.*, 2019) and apparent stress (τ_a; *Picozzi, Bindi, Zollo, et al.*, 2019). Here, we have shown a relationship between δBe and the radiation efficiency η_R. From this perspective, therefore, changes in δBe are important pieces of information that could suggest the identification of key dynamic features of the rupture processes (e.g., related to fluids migration or crack healing affecting η_R).

Figure 5a shows the comparison between the geodetic displacement from the GNSS stations MRCV and MRLC (*D'Agostino et al.*, 2018) and the δBe for both PGA and FAS at different frequencies (i.e., from 1 to 25 Hz). We observe that the MRCV and δBe time series share a similar annual cycle, whereas MRLC shows a multiannual cyclicity.

We quantified the correlation of the δBe time series with the geodetic displacement from the stations MRCV through the Spearman's correlation by splitting the data for different years. Figure 5b shows the temporal evolution of the correlation for the FAS and PGA δBes with MRCV. The correlation is generally positive in the period between 2010 and 2016, it becomes anticorrelated in the 2017, and any form of correlation is lost during and after 2018. *Picozzi et al.* (2021) found a similar level of correlation considering the same geodetic displacement time series and both the source dimension and number of earthquakes.

To further study the temporal evolution of δBe and the geodetic displacement, we perform a time–frequency analysis based on the S transform (*Stockwell et al.*, 1996). Unlike the classical spectral analysis of signals performed with the Fourier transform, a time–frequency analysis such as the S transform provides a view of the temporal evolution of the signal characteristics. Figure 5 shows the results of the S transform analysis for the 90-day sliding average number of events (Fig. 5c), the geodetic displacement for MRCV (Fig. 5d) and MRLC (Fig. 5e), and finally the δBe for PGA (Fig. 5f). In these plots, cycles with a period of 1, 3, and 6 yr are highlighted (red dashed lines).

In agreement with *D'Agostino et al.* (2018), we observe that, for both the number of events and the geodetic displacement at MRCV, the dominant signal has a period corresponding to the annual cycle and lasts for the whole period (Fig. 5c, d). In contrast to the number of events, MRCV shows a second harmonic with a period of 6 yr. The same pluriannual cycle dominates MRLC (Fig. 5e). Interestingly, δBe (Fig. 5f) shows a signal with an annual cycle as MRCV, but only approximately until 2014, which corresponds rather well with the rapid increase in discharge of the Caposele spring (Fig. 1b). We also highlight the presence of a harmonic with a period equal to 3 yr that is not present in the geodetic time series and thus deserves future investigations.

These results suggest that the ground-motion intensity is modulated over time by some physical driving forcing mechanism. Hence, we check if similar temporal patterns appear by also studying the evolution in time of the δBe associated with the main five fault segments in the Irpinia area.

We consider the δBes for hypocentral depths between 7 and 15 km, which represents the depth range in which large magnitude earthquakes typically nucleate in the southern Apennines, and we compute the number of earthquakes per year associated with these segments (Fig. 6a). Figure 6 shows the 90-day sliding average of δBe for the Cervialto, San Gregorio, and Melandro–Pergola faults (Fig. 6b), Ofanto (Fig. 6c), and Marzano (Fig. 6d). The fault segments C, SG, and MP are plotted together because they show a very similar trend (Fig. 6b), which is characterized by an initial increase (2008–2010) followed by a progressive tender decrease. Ofanto also shows a rapid increase in δBe before 2010, but then it appears characterized by high δBes until approximately 2015, when it started to progressively decrease (Fig. 6c). Finally, Marzano shows a peculiar behavior (Fig. 6d). In fact, despite being located between Cervialto and San Gregorio, it shows a change in the signs of δBes (i.e., from positive to negative values) before 2014.

To highlight the differences between the Marzano and Cervialto fault segments, both involved in the
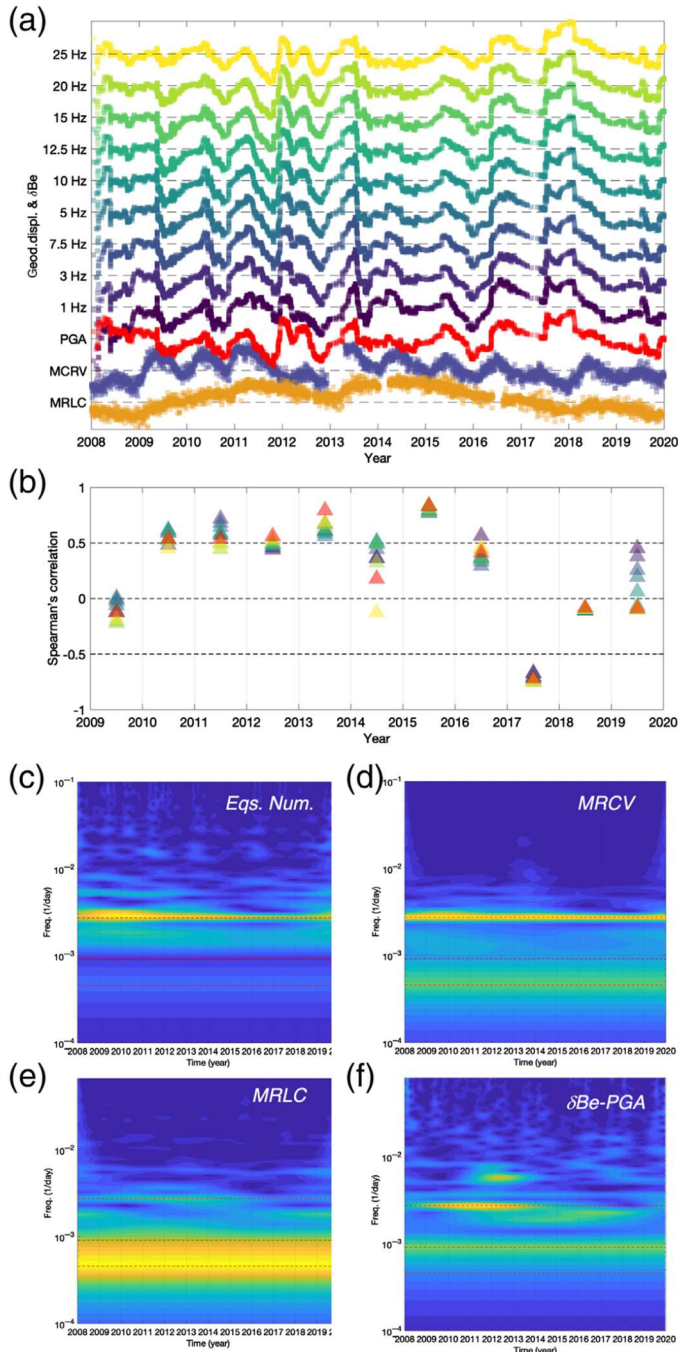
Figure 5 *(a) Temporal evolution of geodetic displacement for the GNSS stations MRLC (orange), MRCV (blue), δBe for PGA (red), and different Fourier amplitude spectrum (FAS) (from blue to yellow). (b) Temporal evolution of the Spearman's correlation coefficient for PGA (red) and different FAS (from blue to yellow) computed with respect to the geodetic displacement of the MRCV station. (c) Time–frequency representation by S transform of the average number of earthquakes calculated in 90-day sliding windows. Frequencies corresponding to 1, 3, 6 yr (dashed red lines). (d, e) Same as (c) but for MRCV and MRLC, respectively. (f) Same as (c) but for δBe. The color version of this figure is available only in the electronic edition.*

main rupture episode of the 1980 Irpinia earthquake, we repeat the time–frequency analysis with the S transform for δBes. Interestingly, in agreement with the geodetic displacement time series, both M and C faults present a 6yr cycle, but Marzano also presents a 2 yr period cycle. Further studies will be done to investigate the nature of the latter cycle.

DISCUSSION

Ground-motion intensity anomalies allow us to depict a different behavior in the segments of the Irpinia fault systems and to capture, after 2013, a change in the spectral signature of earthquakes occurring on the Marzano fault.

The heterogeneity of the Irpinia fault segments is echoed by the spatial distribution of the slope of the Gutenberg–Richter frequency–magnitude relationship (*Gutenberg and Richter*, 1942; *b*-value). The spatial distribution of *b*-value (Fig. 7a, c) is obtained considering the same grid used for δBe but discarding nodes with less than 200 events within 15 km, applying the software ZMAP (*Wiemer*, 2001), and assessing its uncertainty (Fig. 7b, d) with a bootstrap approach (*Efron*, 1979). The *b*-value is interesting because of its inverse linear relation with differential stress (*Amitrano*, 2003; *Bachmann et al.*, 2012) and apparent stress (*Picozzi, Bindi, Spallarossa, et al.*, 2019). We observe that an area with small b-values (∼0.7) is located in correspondence with the Melandro–Pergola fault in the southern sector of the Irpinia area (Fig. 7). The central sector of the investigated area (i.e., corresponding to the Marzano, San Gregorio, and Ofanto fault segments) shows *b*-values close to the median *b*-value of the whole catalog (i.e., 0.9) or slightly lower. Finally, the northern sector (i.e., roughly corresponding to the Cervialto fault) shows the highest *b*-value (i.e., close to 1 and above it). The higher *b*-value in this area agrees with the presence of fluids (i.e., CO_2, see *Improta et al.*, 2014). Unfortunately, the number of events in the catalog does not allow for obtaining 4D b-value images (i.e., spatiotemporal images as done commonly in tomography) with the necessary resolution to reach robust conclusions. However, the high $V_P = V_S$ values in the Marzano fault seen by tomography (*Amoroso et al.*, 2014, 2017; *Improta et al.*, 2014), which are related to a fault-bounded block consisting of fractured and water-saturated Apulian carbonates, could support the higher and fluid related *b*-values in this fault segment compared with Monte–Pergola to
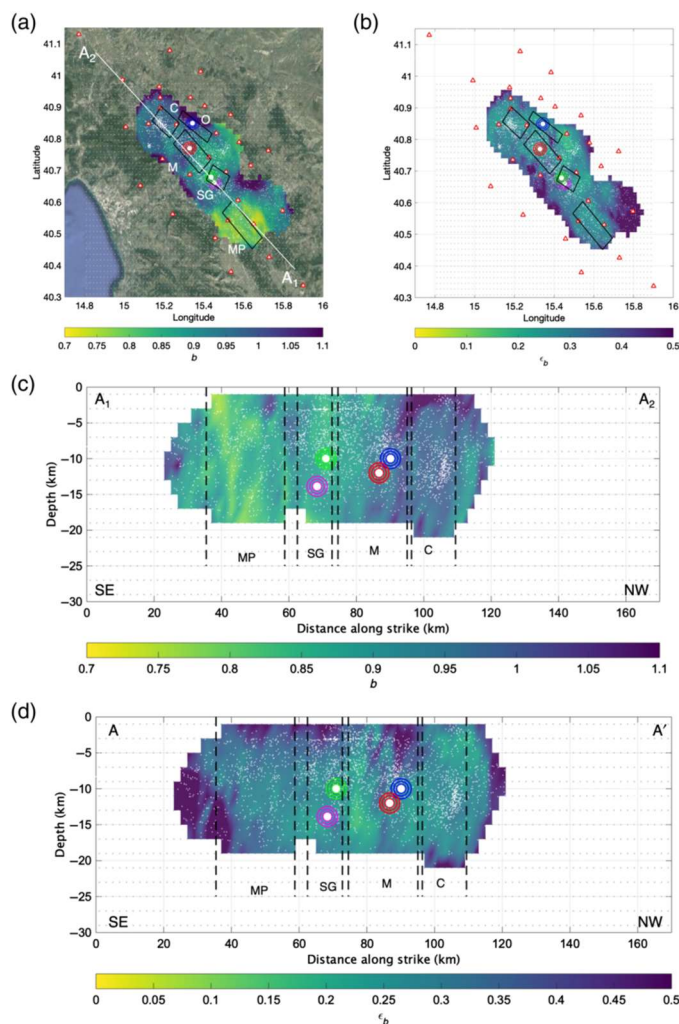
Figure 6 *a) Map showing the spatial distribution of average b-values from bootstrap analysis. (b) The same as (a), but for the relative error on b-value. (c) Contour of the average b-value, from bootstrap analysis, along the strike direction (section A–A′ in Fig. 3a), fault sectors (dashed line), nucleation points for the multi-rupture 1980, M_w 6.9 Irpinia earthquake (dots with circles colored as in Fig. 1a) and epicenter of the 1996, M_w 5.1 Irpinia earthquake (fuchsia dots with circles). (d) The same as (b), but for the relative error on b-value represented along the section A–A′ in Figure 3a. The color version of this figure is available only in the electronic edition.*

the south. Finally, the b-value images suggest an increase of stress going from north to south (Fig. 7a, c).

A summary of the available information and a conceptual scheme of the Irpinia faults system is shown in Figure 8a. For comparison, we also show a schematic view of the 1980 Irpinia earthquake, which nucleated on fault M and developed into two major slip areas, one on fault M and the other on fault C (Fig. 8b).

Looking at the current situation, our results suggest that the Marzano fault is showing time dependencies and is probably influenced by the presence of flu-

ids (high $V_P = V_S$). Even if in a different tectonic context and with much larger spatial scale than that considered in this study, similar observations were found by *Yoshida et al.* (2017) in northeast Japan after the 2011 Tohoku–Oki earthquake, in which microseismicity highlighted significant temporal variations in stress drop. *Yoshida et al.* (2017) associated the stress-drop changes to frictional strength variations, calling into question the role of migrating fluids, not only with respect to the triggering of seismic swarms but also with respect to the dynamics of earthquake ruptures.

As discussed by *Kanamori and Heaton* (2000), the radiative power of faults is related to the friction drop in the initial rupture phases (i.e., from the initial stress to the frictional stress). When friction gradually decreases, a condition that is quite common in small earthquakes (i.e., $M_w < 2$), the fracture energy increases relative to the radiated energy in the case of similar $\Delta\sigma$ (*Kanamori and Heaton*, 2000). This results in a decrease in the radiation efficiency, which we show is inversely proportional to ground-motion intensity (equation 8). We observe that both Cervialto and Melandro–Pergola show small η_R values, suggesting that rupture dynamics in these areas is characterized by gradual decreases in friction. Cervialto hosts a pressurized CO_2-rich reservoir (low $V_P = V_S$; *Improta et al.*, 2014), but it does not show temporal dependencies or evidence of fluid migration.

Recent field, laboratory, and theoretical studies (*Schurr et al.*, 2014; *Socquet et al.*, 2017; *Tape et al.*, 2018) have proposed that earthquakes are preceded by a preparatory phase in which a stable and slow rupture growth develops into an unstable rupture within a confined zone around the future hypocenter. We show that Marzano fault may be consistent with this behavior, for it exhibits significant temporal dependencies consistent with the development of such a preparation phase. The large number of microearthquakes confirms that the fault is not fully locked, and the δBe evolution suggests that the fault has changed its mechanical properties over time. Fluids migration could play a crucial role in driving the future microseismicity to be positively self-organized and thus facilitate the generation of a large earthquake.

In this framework, it is worth mentioning that fluids in karst aquifers following high-multiyear recharge and intense seasonal rainfall can also lead to poroelastic deformation that modulate deeper microseismicity and potentially induce large earthquakes,
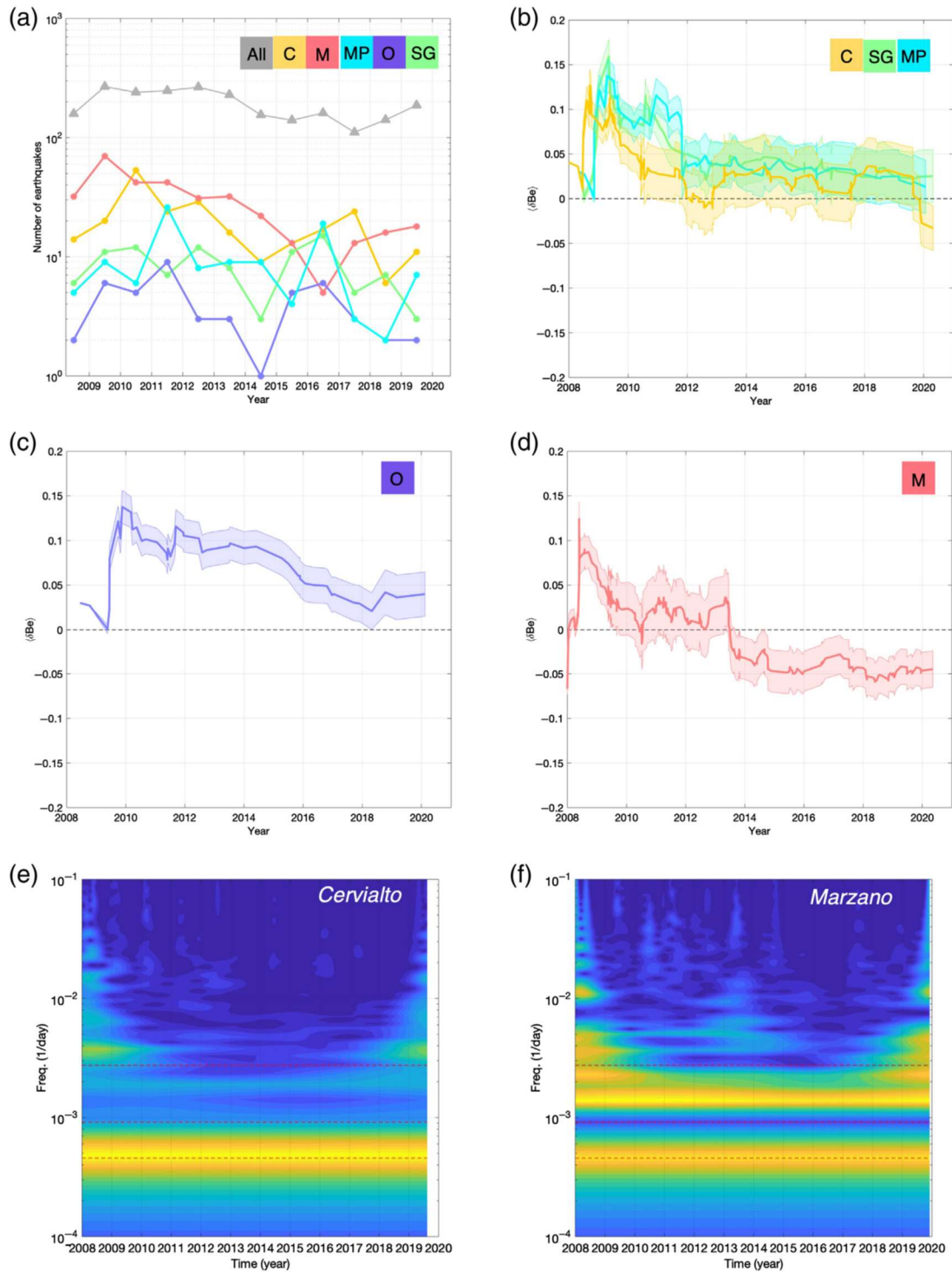
Figure 7 (a) Number of events per year associated with the C-fault (yellow line), M-fault (red line), SG-fault (green line), O-fault (blue line), MP-fault (cyan line), and the whole catalog (gray line). (b) Average δBe calculated in 90-day sliding windows for C, SG, and MP faults. (c) Same as (b) but for O-fault. (d) Same as (b) but for M-fault. (e, f) Same as Figure 5b but for C and M faults, respectively. The color version of this figure is available only in the electronic edition.

as shown by *D'Agostino et al.* (2018). Interesting evidences of the synchronous and asynchronous modulation of seismicity by hydrological loading has been recently presented for Taiwan by *Hsu et al.* (2011). In addition to a direct correlation between seismicity
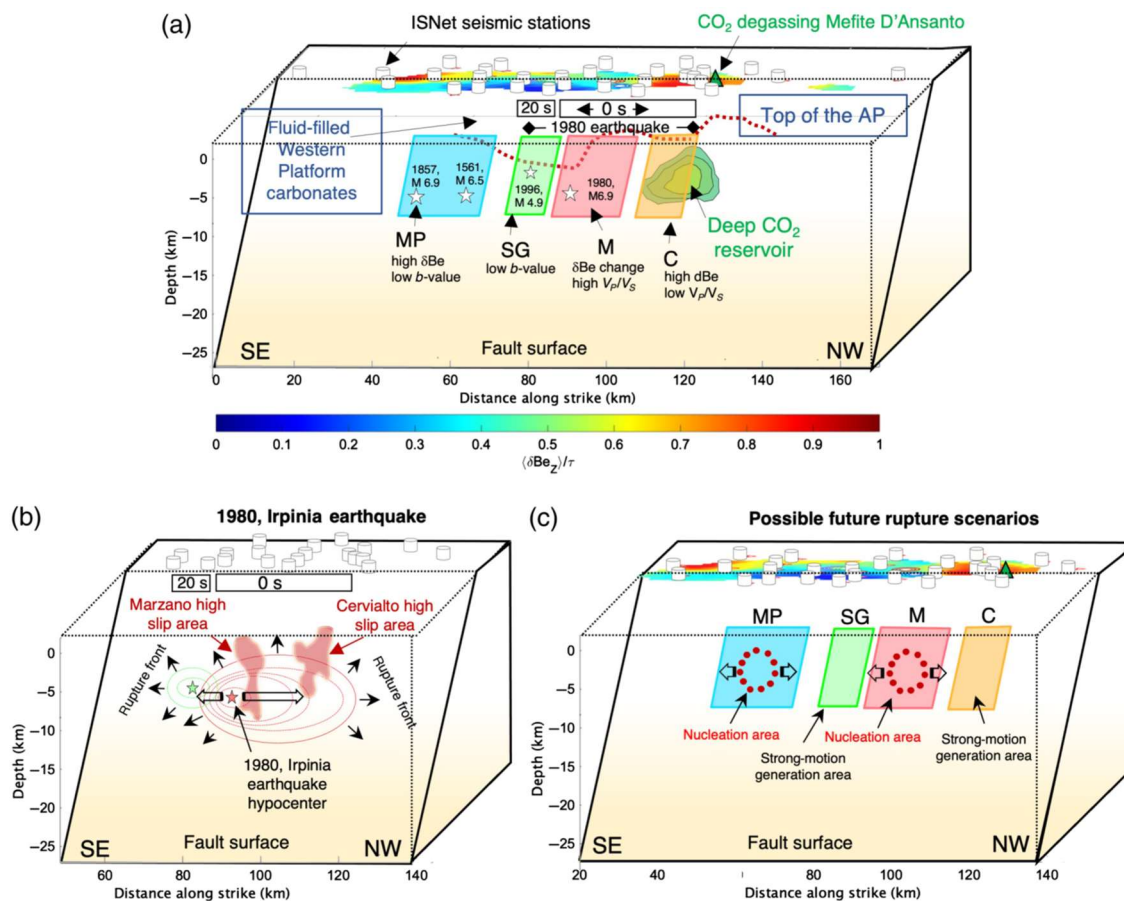
Figure 8 *(a) Outline of the Irpinia faults system with schematic representation of faults (colored as in Fig. 1a), hypocenters of historical and recent large magnitude earthquakes, a few relevant geological information from Improta et al. (2014). ISNet seismic stations (white cylinders), CO₂ degassing site Mefite d'Ansanto (green triangle). (b) Schematic representation of the slip-model inferred by Cocco and Pacor (1993). (c) Example of possible scenario for the next large earthquake in the Irpinia faults system. The color version of this figure is available only in the electronic edition.*

rate and the annual water cycle, this study also found a 3- to 5-month time lag between them. *Hsu et al.* (2011) provide an explanation of these results similar to *D'Agostino et al.* (2018), speculating the role of shallower depth events, influenced by a hydrological forcing, in the triggering of critically stressed faults.

The annual and multiyear cycle that we observe in both geodetic displacement and ground-motion intensity also has been documented in the L'Aquila intra-mountain basin (cycle with repeat time 4–5 yr), an area in the central sector of the Apennine chain (*Devoti et al.*, 2018). The authors invoked the El-Nino Oscillation as the forcing factor, which, according to *Brönnimann* (2007), has a period varying between 3 and 7 yr.

In addition to the multiyear cycle, we note that the Cervialto fault shows a different seismic behavior than the close Marzano, presenting a similar number of events per year (i.e., indicating that the fault is not fully locked and is also slipping), but without temporal

variations being detected. This behavior is consistent with the high *b*-values observed (the stress around the fault is decreasing due to the unlocking) and could be favored by high-pressure CO₂. δ*Be*s are high here because the patches that are pinning the fault plane and resisting to the slip have a high strength. Thus, Cervialto can be interpreted as a conditionally stable area (*Lay et al.*, 2012), which displaces aseismically except when accelerated by failure of adjacent seismic patches and generates high frequencies during sliding because of high-strength patches.

During this interseismic period, both the San Gregorio and Ofanto segments generate few small earthquakes; they are also locked and may act as future asperities. Finally, to the south, the Melandro Pergola fault shows low b-values, suggesting a high level of stress, and periodically generates a relatively small number of earthquakes mostly organized as swarm-like microseismic sequences.

Of course, we cannot exclude the possibility that the next large earthquake in the area will be associated with fault segments other than those we have considered in this work. However, we must also consider that most of the microseismicity recorded by INFO in recent years is clustered in rock volumes associated with the fault segments related to the 1980 Irpinia earthquake and the Melandro–Pergola to the south.

A possible scenario of the next large earthquake involving these fault segments could see the Marzano and Melandro–Pergola play a role as nucleation areas, whereas the other faults would act as strong-motion generation areas (Fig. 8c). Monitoring the temporal evolution and mapping the spatial distribution of ground-motion intensity anomalies is therefore essential to selecting the most likely scenario events for seismic hazard studies (*Ameri et al.*, 2011).

A key result of our study is that ground motion allows us to detect spatial differentiation and time dependency of an active fault system. This is particularly relevant because some of the Irpinia fault segments are in rather advanced stage of their seismic cycle (*Galli and Peronace*, 2014).

Our study demonstrates that monitoring the ground motion can allow for following the temporal evolution of faults. Indeed, in the future, ground-motion intensity could also be used to complement other source parameters and provide useful information for the detailed modeling of fault zones (e.g., *Maury et al.*, 2020). Furthermore, our results suggest that the ground-motion intensity could become important information for approaches similar to the one proposed by *Picozzi and Iaccarino* (2021) aiming at unveiling preparatory processes leading to a large earthquake.

CONCLUSION

We showed that ground-motion intensity allows us to capture temporal dependency affecting the behavior of a specific fault segment, where the 1980 M_S 6.9 earthquake enucleated. Our anatomical study of a high hazard, active fault system reveals that adjacent segments of the Irpinia fault system have different properties and behave in a heterogeneous way. We showed that the fault segments react to the tectonic loading in three different ways: some are silent, others show a significant time-independent microcracking, and others show significant time dependencies both in terms of numbers and characteristics of microearthquakes.

Moreover, we highlighted that ground-motion intensity presents an annual cycle in agreement with independent geodetic displacement observations from a GNSS station in the area. Following the interpretation proposed by *D'Agostino et al.* (2018), the karst aquifers recharge cycle is able to modulate not only the occurrence rate of microseismicity but also its ground-motion characteristics.

Our result is particularly relevant because large earthquakes in Italy develop as multiple rupture episodes in which a large event is followed within seconds to months by large secondary events with magnitudes close to the first mainshock or even larger (*Improta et al.*, 2019). Tools for high-resolution monitoring of faults, based on easily computable parameters as the ground-motion intensity that we present here, are thus urged for seismic risk awareness and preparedness. Our results are precious pieces of information for unveiling the strength and friction properties of the various fault segments and discussing the impact of these variations for the hypocenters and asperities locations of future large earthquakes.

DATA AND RESOURCES

DECLARATION OF COMPETING INTERESTS

ACKNOWLEDGMENTS

REFERENCES

Adinolfi, G. M., S. Cesca, M. Picozzi, S. Heimann, and A. Zollo (2019). Detection of weak seismic sequences based on arrival time coherence and empiric network detectability: An application at a near fault observatory, Geophys. J. Int. 218, no. 3, 2054–2065, doi: 10.1093/gji/ggz248.

Aki, K. (1965). Maximum likelihood estimation of b in the formula log N = a-bM and its confidence limits, Bull. Seismol. Soc. Am. 43, 237–239.

Al Atik, L., A. Abrahamson, J. J. Bommer, F. Scherbaum, F. Cotton, and N. Kuehn (2010). The variability of ground-motion prediction models and its components, Seismol. Res. Lett. 81, no. 5, 794–801, doi: 10.1785/gssrl.81.5.794.

Allmann, B. P., and P. M. Shearer (2007). Spatial and temporal stress drop variations in small earthquakes near Parkfield, California, J. Geophys. Res. 112, no. B04305, doi: 10.1029/2006JB004395.

Ameri, G., A. Emolo, F. Pacor, and F. Gallovič (2011). Ground-motion simulations for the 1980 M 6.9 Irpinia earthquake (Southern Italy) and scenario events, Bull. Seismol. Soc. Am. 101, no. 3, 1136–1151, doi: 10.1785/0120100231.

Amitrano, D. (2003). Brittle-ductile transition and associated seismicity: Experimental and numerical studies and relationship with the b value, J. Geophys. Res. 108, no. B1, 2044, doi: 10.1029/2001JB000680. Amoroso, O., A. Ascione, S. Mazzoli, J. Virieux, and A. Zollo (2014). Seismic imaging of a fluid storage in the actively extending Apennine mountain belt, southern Italy, Geophys. Res. Lett. 41, 3802–3809, doi: 10.1002/2014GL060070.

Amoroso, O., G. Russo, G. De Landro, A. Zollo, S. Garambois, S. Mazzoli, M. Parente, and J. Virieux (2017). From velocity and attenuation tomography to rock physical modeling: Inferences on fluid-driven earthquake processes at the Irpinia fault system in southern Italy, Geophys. Res. Lett. 44, 6752–6760, doi: 10.1002/2016GL072346.

Ascione, A., S. Mazzoli, P. Petrosino, and E. Valente (2013). A decoupled kinematic model for active normal faults: Insights from the 1980, MS = 6.9 Irpinia earthquake, Southern Italy, Geol. Soc. Am. Bull. 125, 1239–1259, doi: 10.1130/B30814.1.

Avallone, A., G. Selvaggi, E. D'Anastasio, N. D'Agostino, P. Pietrantonio, F. Riguzzi, and L. Zarrilli (2010). The ring network: Improvement of a GPS velocity field in the central Mediterranean, Ann. Geophys. 53, no. 2, 39–54.

Bachmann, C. E., S. Wiemer, B. P. Goertz-Allmann, and J. Woessner (2012). Influence of pore-pressure on the event-size distribution of induced earthquakes, Geophys. Res. Lett. 39, L09302, doi: 10.1029/2012GL051480.

Baltay, A. S., T. C. Hanks, and N. A. Abrahamson (2017). Uncertainty, variability, and earthquake physics in ground-motion prediction equations, Bull. Seismol. Soc. Am. 107, 1754–1772, doi: 10.1785/0120160164.

Bates, D., M. Maechler, B. Bolker, and S. Walker (2015). Fitting linear mixed-effects models using lme4, J. Stat. Software 67, no. 1, 1–48.

Ben-Zion, Y. (2019). A critical data gap in earthquake physics, Seismol. Res. Lett. 90, no. 5, doi: 10.1785/0220190167.

Bernard, P., and A. Zollo (1989). The Irpinia (Italy) 1980 earthquake: Detailed analysis of a complex normal fault, J. Geophys. Res. 94, 1631–164.

Bindi, D., R. Castro, G. Franceschina, L. Luzi, and F. Pacor (2004). The 1997–1998 Umbria-Marche sequence (central Italy): Source, path, and site effects estimated from strong motion data recorded in the epicentral area, J. Geophys. Res. 109, no. B04312, doi: 10.1029/2003JB002857.

Bindi, D., F. Cotton, D. Spallarossa, M. Picozzi, and E. Rivalta (2018). Temporal variability of ground shaking and stress drop in Central Italy: A hint for fault healing? Bull. Seismol. Soc. Am. 108, no. 4, 1853–1863, doi: 10.1785/0120180078.

Bindi, D., S. Parolai, H. Grosser, C. Milkereit, and E. Durukal (2007). Empirical ground-motion prediction equations for northwestern Turkey using the aftershocks of the 1999 Kocaeli earthquake, Geophys. Res. Lett. 34, no. 8, doi: 10.1029/2007GL029222.

Bindi, D., M. Picozzi, D. Spallarossa, F. Cotton, and S. R. Kotha (2019). Impact of magnitude selection on aleatory variability associated with ground-motion prediction equations: Part II—analysis of the between-event distribution in Central Italy, Bull. Seismol. Soc. Am. 109, no. 1, 251–262, doi: 10.1785/0120180239.

Bindi, D., D. Spallarossa, and F. Pacor (2017). Between-event and between-station variability observed in the Fourier and response spectra domains: Comparison with seismological models, Geophys. J. Int. 210, 1092–1104, doi: 10.1093/gji/ggx217.

Brenguier, F., M. Campillo, C. Hadziioannou, N. M. Shapiro, R. M. Nadeau, and E. Larose (2008). Postseismic relaxation along the San Andreas fault at Parkfield from continuous seismological observations, Science 321, no. 5895, 1478–1481, doi: 10.1126/science.1160943.

Brönnimann, S. (2007). Impact of El Niño–Southern oscillation on European climate, Rev. Geophys. 45, RG3003, doi: 10.1029/2006RG000199.

Brune, J. N. (1970). Tectonic stress and the spectra of seismic shear waves from earthquakes, J. Geophys. Res. 75, 4997–5009, doi: 10.1029/jb075i026p04997.

Burrato, P., and G. Valensise (2008). Rise and fall of a hypothesized seismic gap: Source complexity in the M_w 7.0 16 December 1857 Southern Italy earthquake, Bull. Seismol. Soc. Am. 98, no. 1, 139–148, doi: 10.1785/0120070094.

Castro, R. R., J. G. Anderson, and S. K. Singh (1990). Site response, attenuation and source spectra of S waves along the Guerrero, Mexico, subduction zone, Bull. Seismol. Soc. Am. 80, no. 6, 1481–1503.

Causse, M., and S. G. Song (2015). Are stress drop and rupture velocity of earthquakes independent? Insight from observed ground motion variability, Geophys. Res. Lett. 42, 7383–7389, doi: 10.1002/2015GL064793.

Chiarabba, C., P. De Gori, M. Segou, and M. Cattaneo (2020). Seismic velocity precursors to the 2016 M_w 6.5 Norcia (Italy) earthquake, Geology 48, doi: 10.1130/G47048.1.

Chiodini, G., C. Cardellini, A. Amato, E. Boschi, S. Caliro, F. Frondini, and G. Ventura (2004). Carbon dioxide earth degassing and seismogenesis in central and southern Italy, Geophys. Res. Lett. 31, L07615, doi: 10.1029/2004GL019480.

Cocco, M., and F. Pacor (1993). The rupture process of the 1980 Irpinia, Italy, earthquake from the inversion of strong motion waveforms, Tectonophysics 218, 157–177.

Cotton, F., R. Archuleta, and M. Causse (2013). What is sigma of the stress drop? Seismol. Res. Lett. 84, 42–48, doi: 10.1785/0220120087.

Courboulex, F., M. Vallée, M. Causse, and A. Chounet (2016). Stress-drop variability of shallow earthquakes extracted from a global database of source time functions, Seismol. Res. Lett. 87, no. 4, 912–918.

D'Agostino, N., F. Silverii, O. Amoroso, V. Convertito, F. Fiorillo, G. Ventafridda, and A. Zollo (2018). Crustal deformation and seismicity modulated by groundwater recharge of karst aquifers, Geophys. Res. Lett. 45, 12,253–12,262, doi: 10.1029/2018GL079794.

De Landro, G., O. Amoroso, T. A. Stabile, E. Matrullo, A. Lomax, and A. Zollo (2015). High-precision differential earthquake location in 3-D models: Evidence for a rheological barrier controlling the microseismicity at the Irpinia fault zone in southern Apennines, Geophys. J. Int. 203, 1821–1831.

Devoti, R., F. Riguzzi, F. R. Cinti, and G. Ventura (2018). Long-term strain oscillations related to the hydrological interaction between aquifers in intra-mountain basins: A case study from Apennines chain (Italy), Earth Planet. Sci. Lett. 501, 1–12.

Douglas, J., and B. Edwards (2016). Recent and future developments in earthquake ground motion estimation, Earth Sci. Rev. 160, 203–219, doi: 10.1016/j.earscirev.2016.07.005.

Efron, B. (1979). Bootstrap methods: Another look at the jackknife, Ann. Stat. 7, no. 1, 1–26.

Fiorillo, F., M. Petitta, E. Preziosi, S. Rusi, L. Esposito, and M. Tallini (2015). Long-term trend and fluctuations of karst spring discharge in a Mediterranean area (central-southern Italy), Environ. Earth Sci. 74, no. 1, 153–172, doi: 10.1007/s12665-014-3946-6.

Gutenberg, B., and C. F. Richter (1942). Earthquake magnitude, intensity, energy, and acceleration, Bull. Seismol. Soc. Am. 32, 163–191.

Hanks, T. C., and R. K. McGuire (1981). The character of high frequency strong ground motion, Bull. Seismol. Soc. Am. 71, 2071–2095, doi: 10.1785/BSSA0710062071.

Hsu, Y.-J., H. Kao, R. Bürgmann, Y.-T. Lee, H.-H. Huang, Y.-F. Hsu, Y.-M. Wu, and J. Zhuang (2011). Synchronized and asynchronous modulation of seismicity by hydrological loading: A case study in Taiwan, Sci. Adv. 7, eabf7282.

Iaccarino, A. G., M. Picozzi, D. Bindi, and D. Spallarossa (2020). On-site earthquake early warning: Predictive models for acceleration response spectra considering site effects, Bull. Seismol. Soc. Am. 110, 1289–1304, doi: 10.1785/0120190272.

Improta, L., P. De Gori, and C. Chiarabba (2014). New insights into crustal structure, Cenozoic magmatism, CO_2 degassing, and seismogenesis in the southern Apennines and Irpinia region from local earthquake tomography, J. Geophys. Res. 119, 8283– 8311, doi: 10.1002/2013JB010890.

Improta, L., D. Latorre, L. Margheriti, A. Nardi, A. Marchetti, A. M. Lombardi, B. Castello, F. Villani, M. G. Ciaccio, F. M. Mele, et al. (2019). Multi-segment rupture of the 2016 Amatrice-Visso-Norcia seismic sequence (central Italy) constrained by the first high-quality catalog of Early Aftershocks, Sci. Rep. 9, 6921, doi: 10.1038/ s41598-019-43393-2.

Kanamori, H., and T. H. Heaton (2000). Microscopic and macroscopic physics of earthquakes, in Geocomplexity and the Physics of Earthquakes, J. B. Rundle, D. L. Turcotte, and W. Klein (Editors), doi: 10.1029/GM120p0147.

Kanamori, H., and L. Rivera (2004). Static and dynamic scaling relations for earthquakes and their implications for rupture speed and stress drop, Bull. Seismol. Soc. Am. 94, 314–319.

Kotha, S. R., D. Bindi, and F. Cotton (2016). Partially non-ergodic region specific GMPE for Europe and Middle-East, Bull. Earthq. Eng. 14, no. 4, 1245–1263.

Kotha, S. R., G. Weatherill, D. Bindi, and F. Cotton (2020). A region-817 allyadaptable groundmotion model for shallow crustal earthquakes in 818 Europe, Bull. Earth Eng. doi: 10.1007/s10518-020-00869-1.

Lay, T., H. Kanamori, C. J. Ammon, K. D. Koper, A. R. Hutko, L. Ye, H. Yue, and T. M. Rushing (2012). Depth-varying rupture properties of subduction zone megathrust faults, J. Geophys. Res. 117, no. B04311, doi: 10.1029/2011JB009133.

Lucente, F. P., P. De Gori, D. Piccini, M. Di Bona, C. Chiarabba, and N. Piana Agostinetti (2010). Temporal variation of seismic velocity and anisotropy before the 2009 MW 6.3 L'Aquila earthquake, Italy, Geology 38, no. 11, 1015–1018, doi: 10.4401/ag-7227.

Madariaga, R. (1976). Dynamics of an expanding circular fault, Bull. Seismol. Soc. Am. 66, 639–666.

Maury, V., J.-M. Piau, and D. Fitzenz (2020). Conditions for triggering seismic ruptures and/or slow slip events in the framework of a poroplastic fault zone model, J. Geophys. Res. 125, e2019JB019273, doi: 10.1029/2019JB019273.

Nielsen, S. (2017). From slow to fast faulting: Recent challenges in earthquake fault mechanics, Phil. Trans. Roy. Soc. Lond. A. 375, doi: 10.1098/rsta.2016.0016.

Oth, A., H. Miyake, and D. Bindi (2017). On the relation of earthquake stress drop and ground motion variability, J. Geophys. Res. 122, 5474–5492, doi: 10.1002/2017JB014026.

Pacor, F., D. Spallarossa, A. Oth, L. Luzi, R. Puglia, L. Cantore, A. Mercuri, M. D'Amico, and D. Bindi (2016). Spectral models for ground motion prediction in the L'Aquila region (central Italy): Evidence for stress-drop dependence on magnitude and depth, Geophys. J. Int. 204, no. 2, 697–718, doi: 10.1093/gji/ggv448.

Pantosti, D., and G. Valensise (1990). Faulting mechanism and complexity of the 23 November, 1980, Campania-Lucania earthquake inferred form surface observations, J. Geophys. Res. 95, no. B10, 15,319–15,341.

Pedregosa, F., G. Varoquaux, A. Gramfort, V. Michel, B. Thirion, O. Grisel, M. Blondel, P. Prettenhofer, R. Weiss, V. Dubourg, et al. (2011). Scikit-learn: Machine learning in Python, J. Mach. Learn. Res. 12, 2825–2830.

Picozzi, M., and A. G. Iaccarino (2021). Forecasting the preparatory phase of induced earthquakes by recurrent neural network, Forecasting 3, 17–36, doi: 10.3390/forecast3010002.

Picozzi, M., D. Bindi, G. Festa, F. Cotton, A. Scala, and N. D'Agostino (2021). Spatio-temporal evolution of microseismicity seismic source properties at the Irpinia near fault observatory, Southern Italy, Bull. Seismol. Soc. Am. doi: 10.1785/0120210064.

Picozzi, M., D. Bindi, D. Spallarossa, A. Oth, D. Di Giacomo, and A. Zollo (2019). Moment and energy magnitudes: Diversity of views on earthquake shaking potential and earthquake statistics, Geophys. J. Int. 216, 1245–1259, doi: 10.1093/gji/ggy488.

Picozzi, M., D. Bindi, A. Zollo, G. Festa, and D. Spallarossa (2019). Detecting long-lasting transients of earthquake activity on a fault system by monitoring apparent stress, ground motion and clustering, Sci. Rep. 9, 16268, doi: 10.1038/s41598-019-52756-8.

Picozzi, M., A. Oth, S. Parolai, D. Bindi, G. De Landro, and O. Amoroso (2017). Accurate estimation of seismic source parameters of induced seismicity by a combined approach of generalized inversion and genetic algorithm: Application to the Geysers geothermal area, California, J. Geophys. Res. 122, doi: 10.1002/2016JB013690.

Piña-Valdés, J., A. Socquet, and F. Cotton (2018). Insights on the Japanese subduction Megathrust properties from depth and lateral variability of observed ground motions, J. Geophys. Res. 123, no. 10, 8937–8956, doi: 10.1029/2018JB015743.

Piña-Valdés, J., A. Socquet, F. Cotton, and S. Specht (2018). Spatiotemporal variations of ground motion in Northern Chile before and after the 2014 M_w 8.1 Iquique Megathrust Event, Bull. Seismol. Soc. Am. 108, no. 2, 801–814, doi: 10.1785/0120170052.

Rabe-Hesketh, S., A. Skrondal, and A. Pickles (2005). Maximum likelihood estimation of limited and discrete dependent variable models with nested random effects, J. Econom. 128, no. 2, 301–323, doi: 10.1016/j.jeconom.2004.08.017.

Scholz, C. H. (2019). The Mechanics of Earthquakes and Faulting, Cambridge University Press, New York, New York.

Schurr, B., G. Asch, S. Hainzl, J. Bedford, A. Hoechner, M. Palo, R. Wang, M. Moreno, M. Bartsch, Y. Zhang, et al. (2014). Gradual unlocking of plate boundary controlled initiation of the 2014 Iquique earthquake, Nature 512, 299–302, doi: 10.1038/nature13681. Socquet, A., J. Piña-Valdes, J. Jara, F. Cotton, A. Walpersdorf, N. Cotte, S. Specht, F. Ortega-Culaciati, D. Carrizo, and E. Norabuena (2017). An 8 month slow slip event triggers progressive nucleation of the 2014 Chile megathrust, Geophys. Res. Lett. 44, no. 9, 4046–4053.

Spallarossa, D., S. R. Kotha, M. Picozzi, S. Barani, and D. Bindi (2019). On-site earthquake early warning: A partially non-ergodic perspective from the site effects point of view, Geophys. J. Int. 216, no. 2, 919–934, doi: 10.1093/gji/ggy470.

Stockwell, R. G., L. Mansinha, and R. P. Lowe (1996). Localization of the complex spectrum: The S transform, IEEE Trans. Signal Process. 44, 998–1001.

Sugan, M., A. Kato, H. Miyake, S. Nakagawa, and A. Vuan (2014). The preparatory phase of the 2009 Mw 6.3 L'Aquila earthquake by improving the detection capability of low-magnitude foreshocks, Geophys. Res. Lett. 41, 6137–6144, doi: 10.1002/2014GL061199.

Tape, C., S. Holtkamp, V. Silwal, J. Hawthorne, Y. Kaneko, J. P. Ampuero, C. Ji, N. Ruppert, K. Smith, and M. E. West (2018). Earthquake nucleation and fault slip complexity in the lower crust of central Alaska, Nat. Geosci. 11, 536–541, doi: 10.1038/s41561-0180144-2.

Uchida, N., and R. Bürgmann (2019). Repeating earthquakes, Annu. Rev. Earth Planet. Sci. 47, 305–332.

Vassallo, M., G. Festa, and A. Bobbio (2012). Seismic ambient noise analysis in southern Italy, Bull. Seismol. Soc. Am. 102, no. 2, 574–586, doi: 10.1785/0120110018.

Wiemer, S. (2001). A software package to analyze seismicity: ZMAP, Seismol. Res. Lett. 72, 373–382.

Wiemer, S., and M. Wyss (2002). Mapping spatial variability of the frequency-magnitude distribution of earthquakes, Adv. Geophys. 45, no. 2002, 259–302, doi: 10.1016/S0065-2687(02)80007-3.

Yoshida, K., T. Saito, Y. Urata, Y. Asano, and A. Hasegawa (2017). Temporal changes in stress drop, frictional strength, and earthquake size distribution in the 2011 Yamagata-Fukushima, NE Japan, earthquake swarm, caused by fluid migration, J. Geophys. Res. 122, 10,379–10,397, doi: 10.1002/2017JB014334.

Zollo, A., A. Orefice, and V. Convertito (2014). Source parameter scaling and radiation efficiency of microearthquakes along the Irpinia fault zone in southern Apennines, Italy, J. Geophys. Res. 119, 3256–3275, doi: 10.1002/2013JB010116.